ADVANCES IN MATERIALS SCIENCE, Vol. 23, No. 4 (78), December 2023

DOI: 10.2478/adms-2023-0023

Dávid Miklós Kemény[1,*], Bence Sándor[1], Balázs Varbai[1], Levente Tamás Katula[1]

[1]*Department of Materials Science and Engineering, Faculty of Mechanical Engineering, Budapest University of Technology and Economics, Budapest, Hungary*

[*]*kemeny.david@gpk.bme.hu*

THE EFFECTS OF ARC VOLTAGE AND SHIELDING GAS TYPE ON THE MICROSTRUCTURE OF WIRE ARC ADDITIVELY MANUFACTURED 2209 DUPLEX STAINLESS STEEL

ABSTRACT

Duplex stainless steels (DSSs) are widely used due to their corrosion resistance. Austenite and ferrite determine the excellent properties. Ferrite provides strength and good corrosion resistance, while austenite provides toughness and weldability. During our research, samples were produced with ER 2209 duplex steel wire using wire arc additive manufacturing (WAAM). Two different 17 V and 19 V arc voltages were used during the production. Two shielding gases were used for each voltage: M12-ArC-2.5 and M12-ArHeC-20/2. The research aimed to determine the ferrite ratio as a function of the welding parameters. The ferrite (or austenite) content must be between 30% and 70% for duplex stainless steel welds, according to the ISO 17781 standard. Based on our research, it can be stated that the austenite ratio increases as the voltage increases, thus failing to fulfill the standard's requirements. The helium content reduced the ferrite ratio even when the 17 V voltage was used due to the gas's higher ionization potential. During the metallographic examination, our welded samples met the standard requirements for the austenite content for 17 V arc voltage and M12-ArC-2.5 shielding gas. The ferrite content in the entire sample cross-section fell between 30-42% during feritscope and image analysis measurements. These welding parameters can be recommended for industrial applications.

Keywords: *wire arc additive manufacturing; duplex steel; ferrite ratio; image analysis*

INTRODUCTION

Stainless steels (SS) can be divided into five groups: austenitic, ferritic, martensitic, precipitation hardenable, and duplex stainless steels [1]. Duplex stainless steels (DSS) are iron-chromium-nickel alloys that combine the favorable properties of ferritic and austenitic stainless steels [2-3]. In terms of their theoretical composition, they are containing 50% ferritic and 50% austenitic [1,3] phases. To achieve this composition, the ferrite stabilizing elements (such as Cr, Mo, Si, W) must be kept in balance with the austenite stabilizing elements (such as Ni, N, Mn) [1,4–6]. The ISO 17781 standard determines the permissible practical composition of duplex steels [7], which is a minimum of 30% and a maximum of 70% of the ferritic (or austenitic) phases [8].

Received 09 Septrmber 2023; Received in revised form 31 October 2023; Accepted 31 October 2023

Most conventional processes can successfully weld DSS. However, in industrial circumstances, arc welding (such as tungsten inert gas welding 141 or gas metal arc welding 135) is used [8–10]. Resistance welding, laser, or electron beam welding techniques can only be used with appropriate compromise [2]. Generally, single- or multi-pass seams are made during the welding of duplex steels. However, in additive manufacturing, multiple layers must be welded on each other. The creation of new layers partially re-melts the already solidified layer below. The new layer (and thermal cycle) reheats the lower layers, which can significantly affect the duplex or non-duplex microstructure.

Layer-by-layer construction is also known as additive manufacturing (AM). Robotic welding can also be implemented to achieve better quality, thus excluding the uncertainty arising from the human factor. This combined process is called WAAM (Wire Arc Additive Manufacturing), a wire-based form of directed energy construction [11]. An electric arc is used to create fusion layer by layer. The welding material is fed into the arc in a controlled manner, which melts entirely due to the high temperature, while the previously deposited layer partially melts. The advantage of WAAM is in the increased productivity and favorable price of the equipment compared to other additive technologies [4,9,12,13]. It is widely used in industry to produce unique or monumental equipment (for example, propellers (WAAMpellers) and crane hooks based on Taşdemir et al. [14]) [15], where a traditional casting process is not feasible or would be much more expensive [16]. In addition to the advantages, there are also disadvantages.

It should be noted that the achievable surface accuracy is ±0.2 mm, and post-processing can often take place [13]. In addition, controlling the heat input is also a serious challenge. Several research deal with this investigation. M. Eriksson et al. [17] investigated the applicability of ER 2594 super duplex wires. The used shielding gas was 97.97% Ar, 2% CO_2 and 0.03% NO. It was found that the increasing heat input resulted in decreasing yield strength and tensile strength while the formability properties increased.

V.A Hosseini et al. [18] made the studies of WAAM of duplex stainless steel blocks welded with ER 2209 wire. They determined the relation between the as-welded microstructure and the thermal cycles. The low heat input, low interlayer temperature sample had an 8% higher austenite ratio than the high heat input, high interlayer temperature sample. N. Knezovic et al. [19] investigated the WAAM of Avesta 2205 wires, using 98% Ar and 2% N_2 shielding gas. The interlayer temperatures were 50°C, 100°C and 150 °C. The ferrite ratio was the highest in the samples with the lowest interlayer temperature, but the process resulted in more porosity than the others. X. Bi et al. [20] examined the 2205 duplex steel wires using cold metal transfer during WAAM. They measured decreasing ferrite content from the substrate to the top of the sample, while the austenite content was increased at the expense of ferrite. A. Queguineur et al. [21] investigated G2209 and G2205 duplex steel wires in WAAM, using CMT technology. The shielding gas was ArHeCO_2N-5/1.8/1.7. The welded G2209 steel sample resulted in a lower ferrite content of 29.69% ± 0.56%. They used three interlayer temperatures: 100°C, 150°C, and 250°C. Zhang Y et al. [22] examined the WAAM of E2209 DSS with pure CO_2 shielding gas. The average austenite content was 74% in the samples, which does not fulfill the standards' requirements.

Reviewing previous research, there was no consensus regarding the use of shielding gas. In all cases, there were different shielding gases, although the shielding gas can significantly influence the heat input and microstructure.

During our research, 4 test specimens were produced using WAAM technology. The manufactured samples were prepared with two different voltages and two different protective gases. To determine the effect of the heat input and the shielding gas on the microstructure of the produced multilayer duplex steel specimens. The metallographic test was carried out during the investigation to analyze the microstructures. The aim of the research was to determine if the ferrite content remained in the desired 30% to 70% range.

MATERIALS AND METHODS

Substrate, welding wire, and the welded specimens

The additive manufacturing process was made on a 300x250x20 mm (W x L x H mm) size S235 JR carbon steel substrate. Böhler G 22 9 3 NL (ER 2209) standard duplex filler wire [23] in 1.2 mm diameter was used during the welding. Table 1 shows the chemical composition of welding wire, and Table 2 shows the mechanical properties according to the manufacturer's datasheet. The Fig. 1 represents the created welded specimens.

Table 1. *The chemical composition of ER 2209 wire, according to the datasheet*

Wire	Chemical composition (weight %)						
	Cr	Ni	Mo	N	Mn	C	Fe
ER 2209	22.5	8.8	3.2	0.15	1.7	≤0.015	Balance

Table 2. *The ER 2209 mechanical properties, according to the datasheet*

Wire	Mechanical property (minimum)		
	Rp0.2 (MPa)	Rm (MPa)	A (%)
ER 2209	min. 450	min. 550	min. 20

Fig. 1. Welded specimens on the substrate

Parameters of welding

The WAAM-produced specimens were made with a Yaskawa Motoman type MA1400 welding robot and Lincoln Power Wave type i400 power supply. The welding gun was perpendicular to the substrate, and the contact tip was at a 12 mm distance from the surface. The M12-ArC-2.5 and M12-ArHeC-20/2 [24] recommended shielding gases were used [25–27]. The shielding gas flow rate was 15 liter/min in every case. Table 3 shows the additional welding parameters and the specific heat input with 0.8 thermal efficiency. It will be referred to later in the text as C_17, C_19, He_17, and He_19 according to the Table 3. The first letter refers to the shielding gases, and the following number refers to the set-up value of the arc voltage. All specimens had 150°C interlayer temperatures, which were monitored with a Testo Technotherm 9500 type thermometer. The samples welded with 17V arc voltage were built up with the size of approximately 220x15x75 mm (LxWxH) and the others with 19V arc voltage were made with approximately 220x20x85 mm size. For the C_17 and He_17 specimens one layer consisted of 5 passes. One pass was 4 mm width, and the overlap distance was 2 mm. For the C_19 and He_19 specimens one layer consisted of 5 passes.

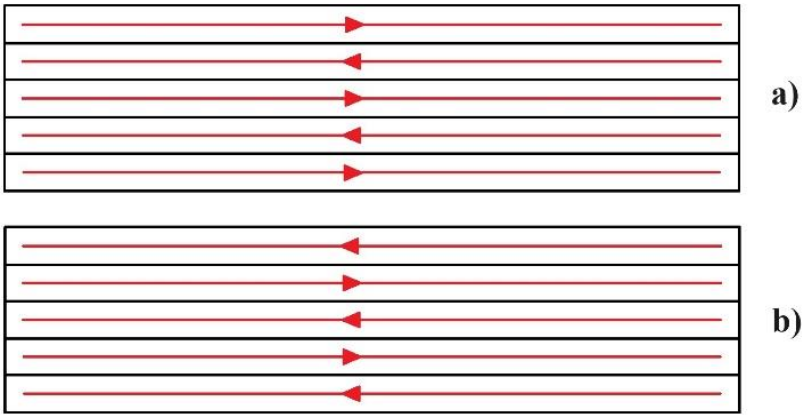

Fig. 2. The direction of laying the seams per layer: a) first layer, b) second layer

Table 3. *The welding parameters during the wire arc additive manufacturing*

Wall	C_17	C_19	He_17	He_19
Shielding Gas	M12 – ArC – 2.5	M12 – ArC – 2.5	M12 – ArHeC – 20/2	M12 – ArHeC – 20/2
Travel Speed (cm/min)	50	50	50	50
Wire Feed (m/min)	3.8	3.8	3.8	3.8
Welding Current (A)	124	142	124	142
Arc Voltage (V)	17	19	17	19
Specific Heat Input (kJ/mm)	0.26	0.34	0.26	0.34
Overlap Distance (mm)	2	3	2	3

One pass was 6 mm width, and the overlap distance was 3 mm. The Fig. 2 a) shows the path of the welding torch. The Fig. 2 b) shows almost the same route, but the direction is opposite. The red lines mean the welding rows and the narrows represent the welding directions. These first two layers are continuously repeated, shifted in the "z" coordinate direction until the welded sample is completed. The 19V welded specimens were made of 34 layers, and the 17V welded specimens were made of 24 layers. The welded pieces will be referred to as walls in the following text.

Microstructure evaluation

The walls were removed from the substrate. It should be noted, that the walls could not have been cut directly from the substrate. An average of 3 layers remained on the substrate by the 17V walls, which means that approximately the remaining 21 layers were examined. In the case of 19V walls, an average of 4 layers remained on the substrate and approximately 30 layers were examined. In the next step, 10 mm thick samples were cut out from the front of the walls, according to Fig. 3.

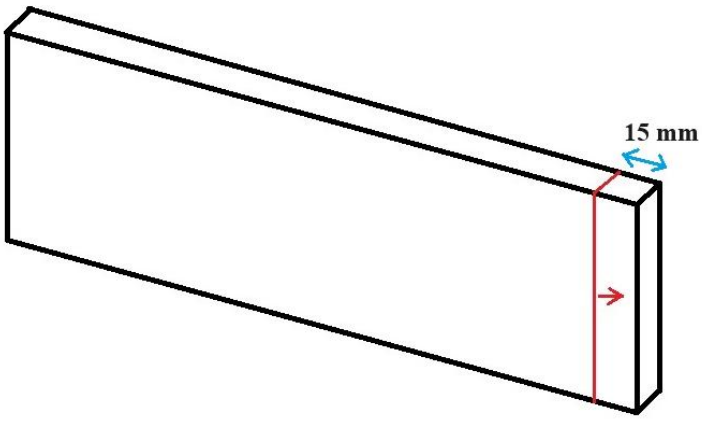

Fig. 3. Location of the removed part

The cut samples were grinded with SiC papers, starting with P80 paper till P4000. The polishing was made with Buehler MetaSerc type 250 equipment using diamond suspension till 1 µm for a better surface. The polished surfaces were cleaned with ethanol, and the etching process continued for 10 seconds. The etchant was Beraha II (85 mL H_2O, 15 mL HCl and 1 g $K_2S_2O_5$) to reveal the two-phase ratio (the ferrite and the austenite). Sulfur dioxide forms a film on the surface of the duplex steel and colors the ferrite grains dark, while leaving the austenite grains unchanged because the solubility of sulfur in the ferrite phase is significantly higher than in the austenite phase [28]. The prepared samples can be seen in Fig. 4 with mosaic pictures. It is necessary to note that there is a fusion failure in the interior of the samples despite the fact that the surface was cleaned with a wire brush after each layer. The Fig. 4 a) is the C_17, the b) is the C_19, the c) is the He_17, and the d) is the He_19 sample.

The polished and etched samples were first photographed with an Olympus SZX16 stereomicroscope. To get higher magnification Olympus PMG-3 type light optical microscope was used. Using a light optical microscope allowed higher magnification and better contrast,

allowing the phase ratio to be determined. For image processing, MathWorks® MATLAB software was used.

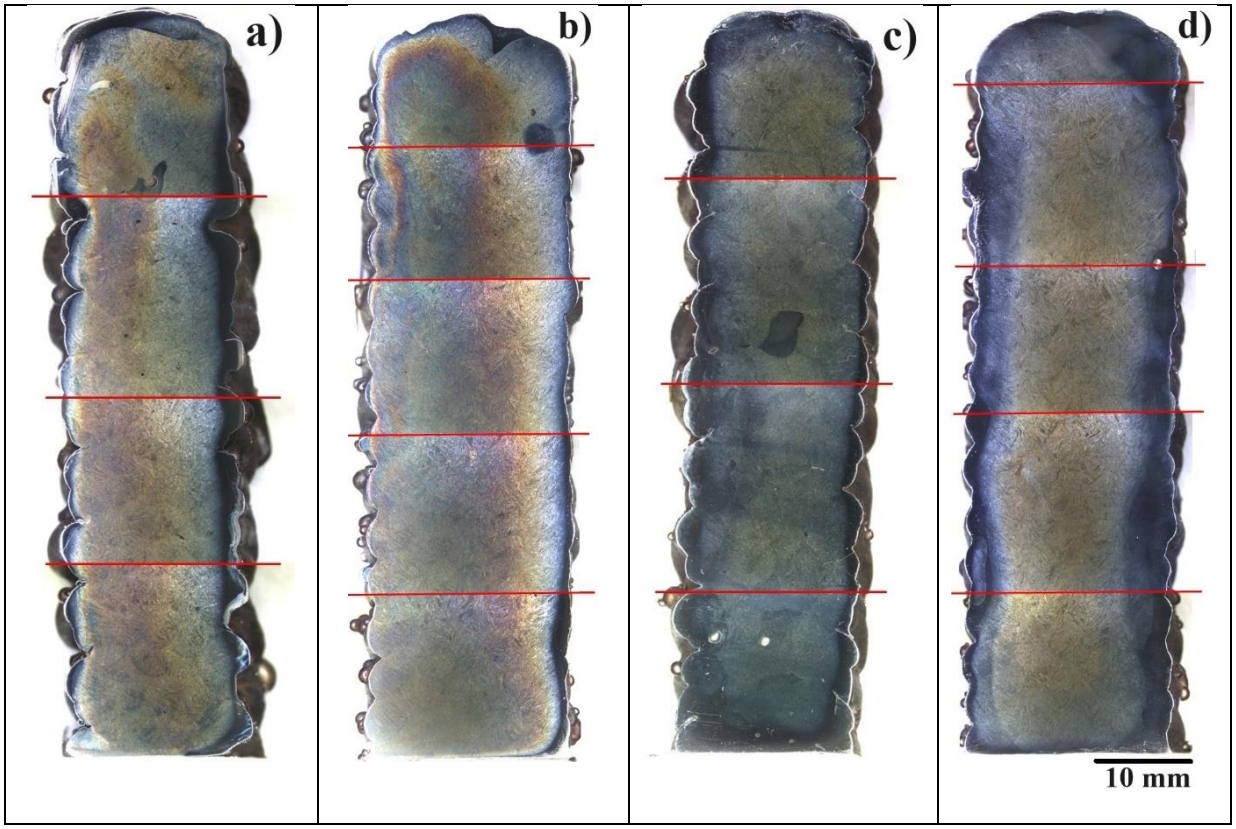

Fig. 4. The additive manufactured 2209 samples after etching a) C_17, b) C_19, c) He_17, d) He_19

The ferrite ratio was also measured with Fischer FMP30 Feritscope. The feritscope has a larger measured volume to be measured comparing to the metallographic techniques [29]. It should be noted that the feritscope measures a larger average volume, while the optical microscope provides a 2D image of a 1.7x1.7 mm area in our case. For this reason, the results of the image analysis and the feritscope measurements cannot be directly compared, but their trend is similar.

The Vickers hardness of the samples was measured by Buehler Indentamet type 1100 equipment. The load was 1 kg, and the dwell time was 12 seconds to meet the requirements of the ISO 6507-1[30] standard.

The methods of image processing

The evaluation was done in MATLAB's with a self-created code. After importing the image, unwanted elements (scratches, size scale) can be selected in the program, which will not be considered during the evaluation. After that, the program creates a grayscale image and determines the highest and lowest intensity pixels. The difference between the two extreme values of intensity gives the contrast; the higher this number, the more suitable the recording is for analysis since the two phases are better separated from each other (equation 1). In the next step, the program converts the image into binary format, for which a limit value must be defined, below which each pixel takes on the value 1 (black) and above the value 0 (white).

The threshold value was determined by adding half of the contrast to the smallest intensity value (total RGB (red, green, blue) intensity). The obtained value must be divided by 256 (equation 2). It is necessary because the image was converted to binary format, which contains values between 0-1 for each pixel according to their intensity.

$$\Delta G = I_{max} - I_{min} \tag{1}$$

$$T = (I_{min} + 0.5 \cdot \Delta G)/256 \tag{2}$$

where:

- ΔG: the difference between the extreme values of the intensity (-)
- Imax and Imin: the maximum and minimum values of the intensity of the pixels in the examined image (-)
- T: limit value

During the first image processing, it was seen that the quality of the binary images could still be improved, so Otsu's method was used [31], which determines the limit based on the distribution function of the pixel intensities. The essence of the process is that in the case of two classes (currently the ferrite and austenite phases), find the limit value where the value of the interclass standard deviation is the smallest. The interclass standard deviation can be defined as the weighted average of the standard deviations of the two classes (equation 3).

$$\sigma_{\omega}^2(t) = \omega_0(t)\sigma_0^2(t) + \omega_1(t)\sigma_1^2(t) \tag{3}$$

where:

- $\sigma_{\omega}^2(t)$: The interclass standard deviation (-)
- $\sigma_{0,1}^2(t)$: standard deviations of classes (-)
- $\omega_{0,1}(t)$: the weight functions belonging to the two classes
- t: limit value (-)

RESULTS AND DISCUSSION

The marking system was added to the samples as seen in Fig. 5. For each sample, the 0 point of the coordinate system was placed in the lower left corner on the side where the sample was removed from the substrate. Each sample was divided into 5 equal parts along its height (y-axis). Moving away from the substrate, the division was made along the y-axis from 1 to 5.

From point 0 of the coordinate system, the samples were also divided horizontally along the x-axis. The 17V samples were divided into 3 equal parts (a, b and c) due to their narrower nature, while the 19V samples were divided into 4 equal parts (a, b, c and d). These divisions designate parts of the surface, which will later be called: box, boxes.

The ferrite content was measured in all boxes along the x and y axes.

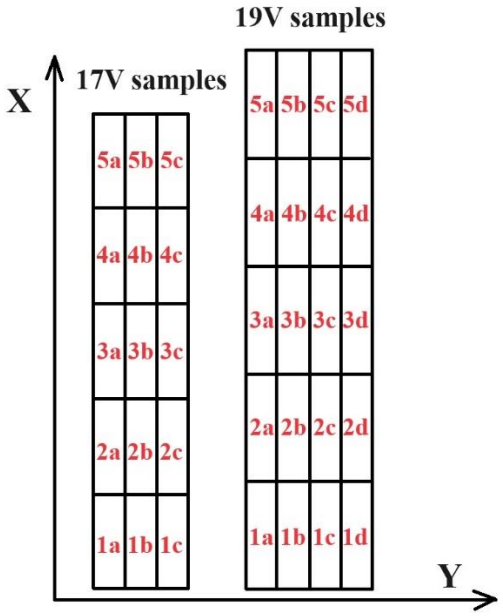

Fig. 5. The marking system of the samples

The comparison of the two types of image processing methods

Image analysis can be influenced by the following: subjectivity, the selected area, the etchant, and the method, etc. It is worth using only one practice during the research for the best possible results due to reproducibility. The Fig. 6 shows the original image of the ER 2209 DSS microstructure, and the converted black and white pictures can be seen in Fig. 7. In Fig. 7 a), the first applied intensity extreme value method and in Fig. 7 b) the Otsu's method can be seen.

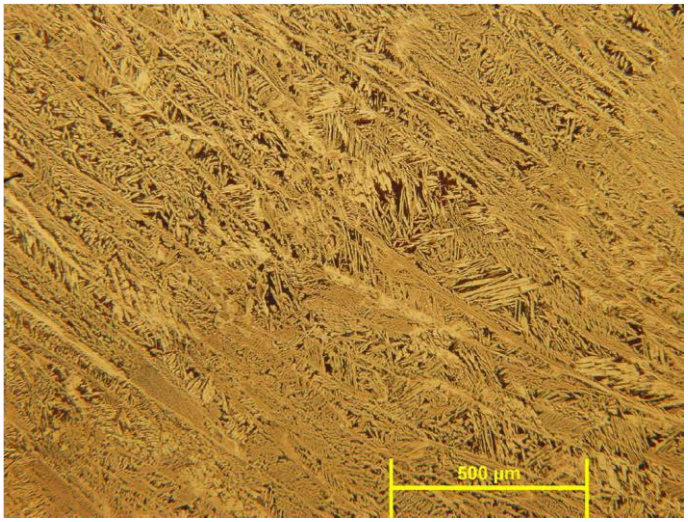

Fig. 6. Microstructure of ER 2209 duplex steel by WAAM

The calculated limit value with the first method was 0.5156. The corresponding ferrite ratio was 39.4%. Otsu's method gave a limit value of 0.4706, which resulted in a ferrite ratio of 28.7%. The second, Otsu's method, proved the best value because it is the closest to the feritscope measurement with a value of 28.5%.

The Otsu's method was used during the evaluation because it provides a better fit than the values measured with the feritscope. In our practice, using Otsu's approach, the limit value typically varied between 0.45-0.55 during the evaluations.

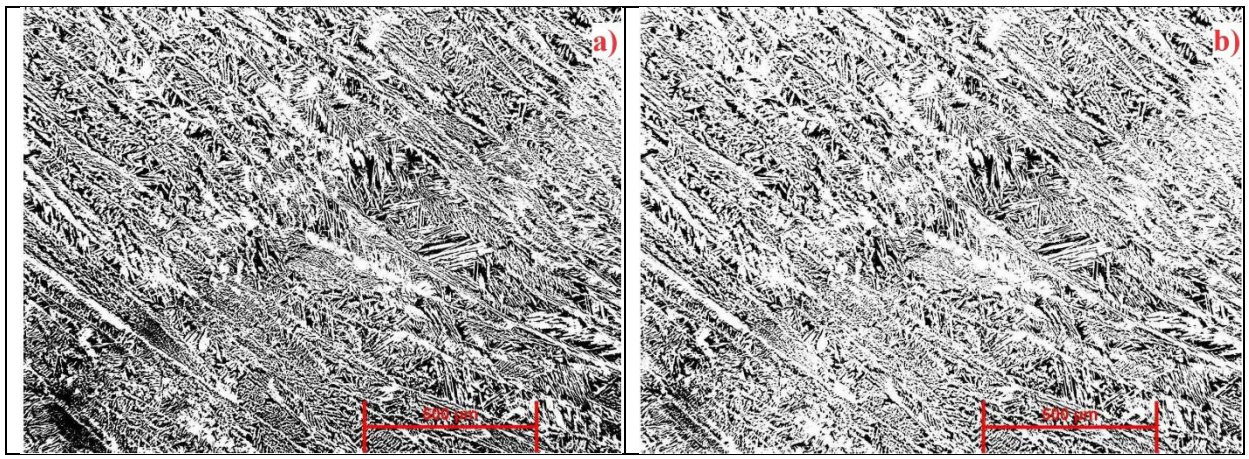

Fig. 7. The binary images of the microstructure seen in Fig 6. a) first image analysis, b) using Otsu's method

The results of the metallographic analysis of the sample welded with 2.5% CO_2 containing shielding gas and 17V arc voltage (sample C_17)

The measured ferrite content can be seen in Tables 4-7. The letters "a, b, c" represent the feritscope results, and the "a*, b*, c*" represent the image analysis results. Only one metallographic picture was analyzed in each box, representing the most characteristic area. Table 4 shows that the ferrite content is the highest close to the substrate, and the content decreases to the 4th line boxes of the sample, after that, it rises again. This is because the heat dissipation of the substrate is still significant at the beginning. The further layer and their subsequent thermal cycle results in a lower cooling rate and thus, the ferrite content is decreasing. In the last layers, the effect of reheating decreases, which increases the amount of ferrite.

Table 4 summarizes the mean values measured along the width and their standard deviation. Fig. 8 shows the average values and standard deviations of ferrite content depending on the box place of sample C_17.

Table 4. *Ferrite content of the C_17 sample measured with feritscope and analyzed with Otsu's image process*

		Sample location among the width					
		a	a*	b	b*	c	c*
y-axis	5	32.6	34.1	33.1	37.0	34.2	36.6
	4	30.8	34.2	32.7	33.9	30.9	34.5
	3	32.1	40.1	31.8	39.1	31.3	37.2
	2	36.1	38.7	40.3	38.7	35.5	39.9
	1	41.5	42.8	43.1	42.4	39.8	42.9

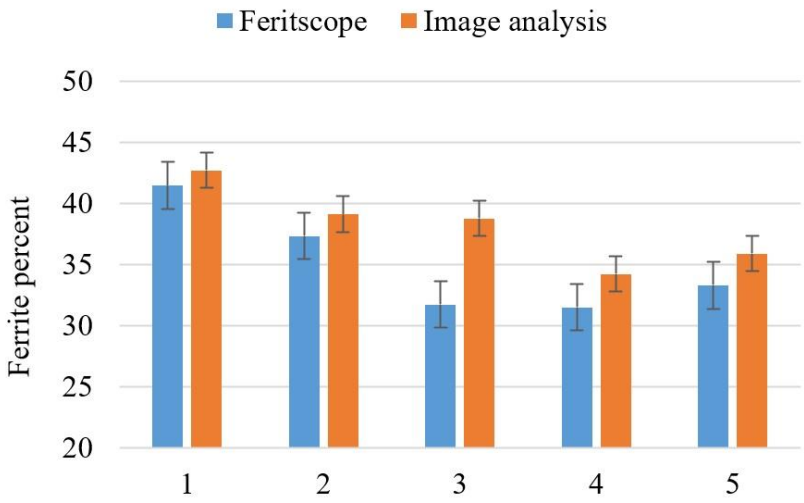

Fig. 8. The average values and standard deviations of ferrite content depending on the height of sample C_17

In the section of sample C_17, the austenite can be found in a lamellar morphology (see Fig. 9), as well as in a dendritic arrangement (see Fig. 10).

Dendritic-shaped austenite was found in the whole sample except in the 3c box, where a lamellar arrangement was found. This shape is characteristic of the Widmanstätten austenite, which forms at the grain boundaries and then grows inside the grains due to further cooling [32].

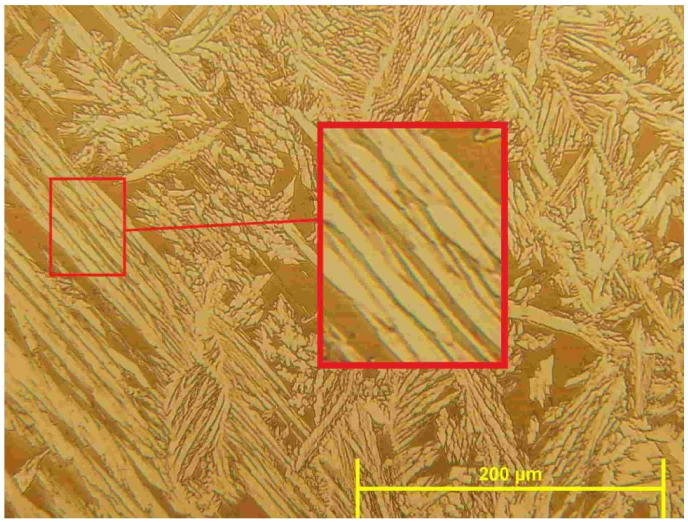

Fig. 9. ER 2209 duplex steel microstructure highlighted the lamellar morphology with red rectangle. The lighter phase element represents the austenite and the darker one is ferrite

Another exciting form of austenite can be seen in Fig. 10 highlighted by a red rectangle. A formation that resembles a smaller grain arrangement is called secondary austenite, which forms due to the reheating of the subsequent passes [1], [32].

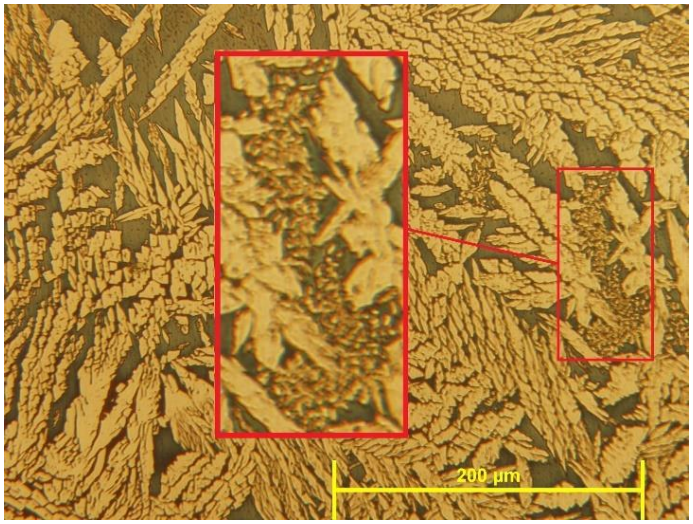

Fig. 10. Characteristic appearance of secondary austenite in C_17 sample first layer

The results of the metallographic analysis of the sample welded with 2.5% CO_2 containing shielding gas and 19V arc voltage (sample C_19)

A similar trend can be seen in the results of sample C_19 in Table 5 and Fig. 11. The ferrite content starts to decrease from the substrate side, then the ferrite ratio increases again at the 5th line boxes of the sample.

Table 5. *Ferrite content of the C_19 sample measured with feritscope and analyzed with Otsu's image process*

		Sample location among the width							
		a	a*	b	b*	c	c*	d	d*
y-axis	5	30.7	34.3	29.7	33.6	28.9	32.1	31.6	33.5
	4	31.2	26.8	28.5	28.7	29.4	29.0	30.6	28.9
	3	31.0	27.1	28.4	30.3	28.6	28.4	31.6	29.6
	2	30.6	27.7	29.5	29.8	28.6	30.0	30.6	29.5
	1	32.3	29.0	32.2	28.3	31.2	32.2	32.6	34.1

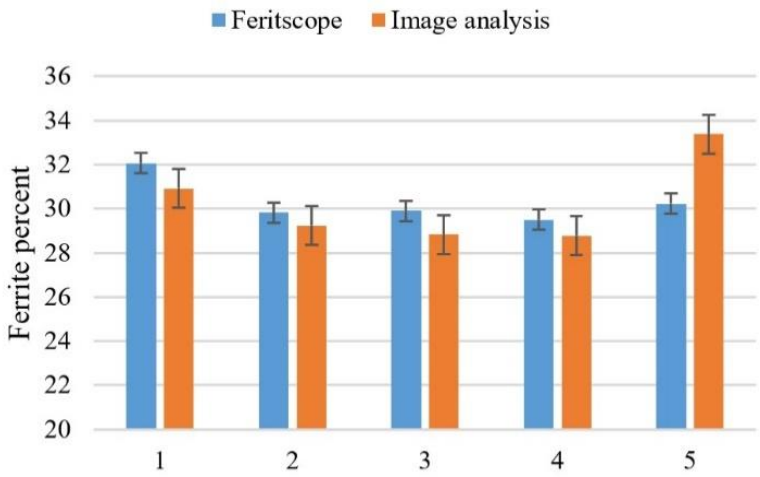

Fig. 11. The average values and standard deviations of ferrite content depending on the y-axis by C_19 wall

The results of the metallographic analysis of the sample welded with 20% He and 2% CO_2 containing shielding gas and 17V arc voltage (sample He_17)

The ferrite ratio, like before, starts to decrease slightly, and in the 5th zone boxes of the sample, it starts to increase again (Fig. 12).

Table 6. *Ferrite content of the He_17 sample measured with feritscope and analyzed with Otsu's image process*

		Sample location among the width					
		a	a*	b	b*	c	c*
y-axis	5	32.0	38.1	33.4	43.4	33.2	42.9
	4	30.6	36.3	30.0	39.4	34.7	38.7
	3	29.8	38.1	29.0	31.5	33.2	37.1
	2	28.1	37.5	29.3	34.2	33.3	35.3
	1	32.2	38.8	33.4	34.1	37.0	38.8

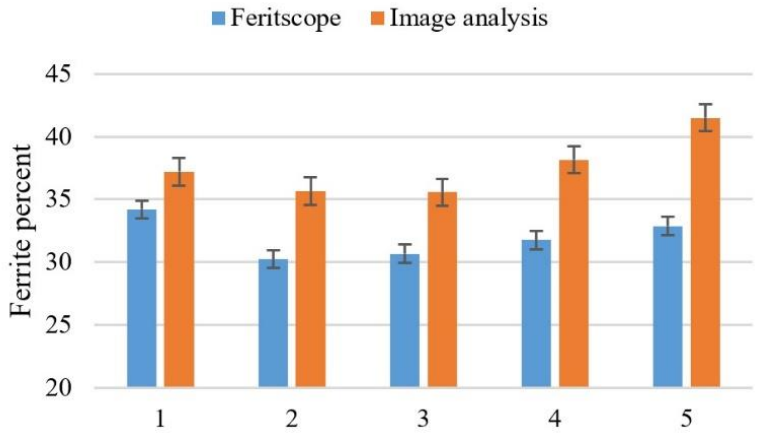

Fig. 12. The average values and standard deviations of ferrite content depending on the y-axis by He_17 wall

The average higher ferrite ratio of 4th line boxes in Table 6 along the width is due to the significant difference in image "3b*" and "4b*" boxes results. A dense arrangement of austenite with few ferrite grains can be seen in Fig. 13 (3b), and large ferrite grains can be seen in Fig. 14 (4b). The amount of secondary austenite is few of these microstructure pictures.

The image of "3b" box is in the middle of the sample, where the amount of heat removal is the smallest. This result is worth comparing with the C_17 sample, where the equilibrium in the heat input was reached in higher layers; in this wall, it can be seen the highest austenite content at the 2nd line boxes (the ferrite content was the minimum heat). The average highest ferrite ratio can be seen at the 5th line boxes.

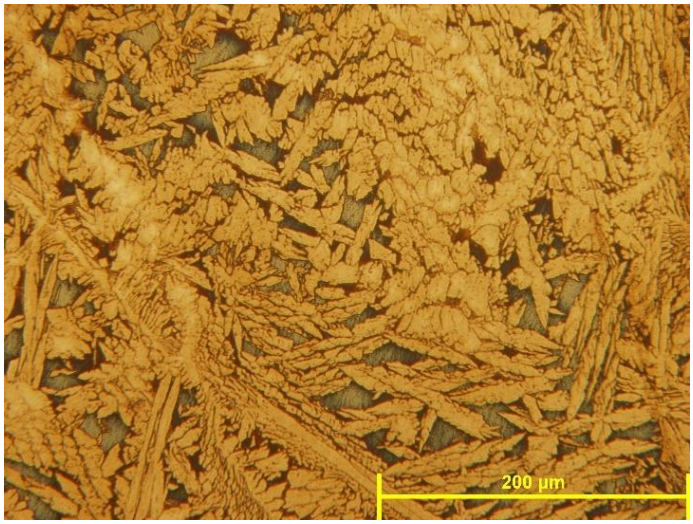

Fig. 13. Higher austenite content of He_17 sample in 3b box

Fig. 14. Higher ferrite ratio of He_17 sample in 4b box

The results of the metallographic analysis of the sample welded with 20% He and 2% CO_2 containing shielding gas and 19V arc voltage (sample He_19)

The ferrite ratio decreases from the substrate and in the 5th zone boxes, it starts to increase again, what are represented in Table 7 and Fig. 15.

Table 7. *Ferrite content of the C_17 sample measured with Feritscope and analyzed with Otsu's image process*

		Sample location among the width							
		a	a*	b	b*	c	c*	d	d*
y-axis	5	29.8	36.3	28.4	32.9	29.8	28.6	28.5	32.6
	4	29.0	22.1	27.0	26.7	27.7	25.4	28.6	22.9
	3	30.6	23.0	30.4	24.7	30.2	27.5	30.2	28.1
	2	30.5	33.6	31.2	29.5	30.9	27.6	31.0	29.1
	1	31.4	32.9	32.3	29.3	34.2	33.9	33.1	36.3

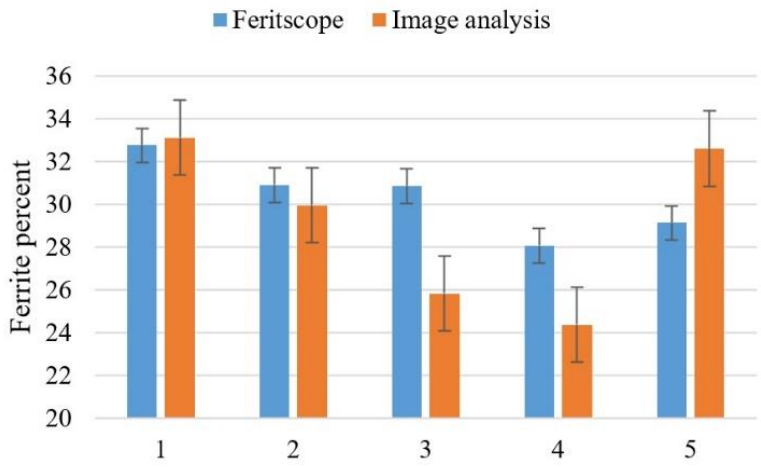

Fig. 15. The average values and standard deviations of ferrite content depending on the y-axis by He_19 wall

Large austenite grains are visible in the 4d box (Fig. 16), presumably, at this height, the cooling time was the longest [1].

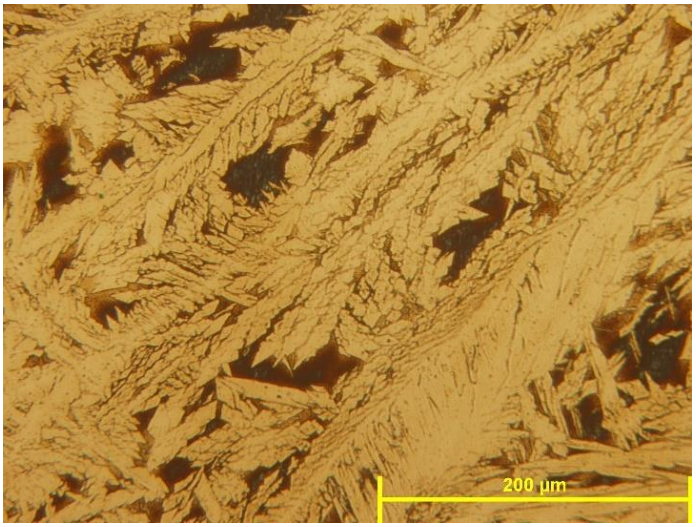

Fig. 16. Coarser austenite formation in the 4d box of the He_19 sample

The ferrite content increases significantly in the 5th line boxes. Finer austenite grains can also be seen in the microscopic image (Fig. 17), and the ferrite grains are more extensive.

It can be noted that the speed of cooling has a significant influence on the resulting microstructure. The cooling rate mainly depends on the heat input, interlayer temperature, preheating, and the wall thickness of the material. The wire material and the shielding gas also determine the resulting microstructure. It can be established that the higher the alloy content, the lower the maximum permissible heat input, and the higher the nitrogen content results in a lower permissible heat input, based on previous research such as L. Karlsson [33] and J. Lippold et al. [1].

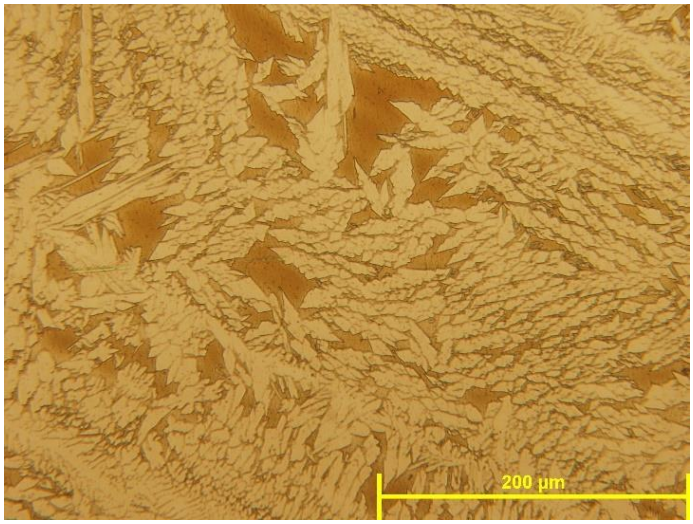

Fig. 17. In the 5a box with finer austenite grains and more ferrite content by He_19 sample

EXAMINATION OF THE EFFECT OF WELDING PARAMETERS

Effects of the used shielding gases

The ferrite ratio was compared with the two different Ar+CO_2 and Ar+He+CO_2 shielding gases with 17V and 19V voltage.

The ferrite content was higher at the wall made with M12–ArC–2.5 type shielding gas by a voltage setting of 17V. Both were obtained from image analysis and feritscope measurements (Fig. 18). The standard deviation of the ferrite percentage of the C_17 sample fell between 0.3 and 2.7, while the standard deviation of the ferrite percentage of the He_17 sample fell between 0.7 and 2.7.

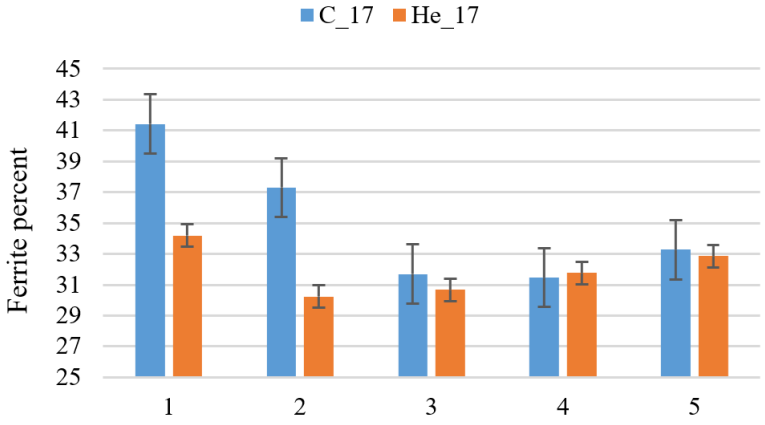

Fig. 18. Comparing the average values of ferrite ratio on the same 17V voltage with different shielding gas by the C_17 and He_17 samples

In Fig. 19, with 19V voltage, it can be seen that the two different gases have almost the same ferrite amount until the third y-axis point. The standard deviation of the ferrite percentage of the C_19 sample fell between 0.6 and 1.9, while the standard deviation of the

ferrite percentage of the He_19 sample fell between 0.3 and 1.2. In the upper layers, it can be seen that the gas with helium content has much more austenite content.

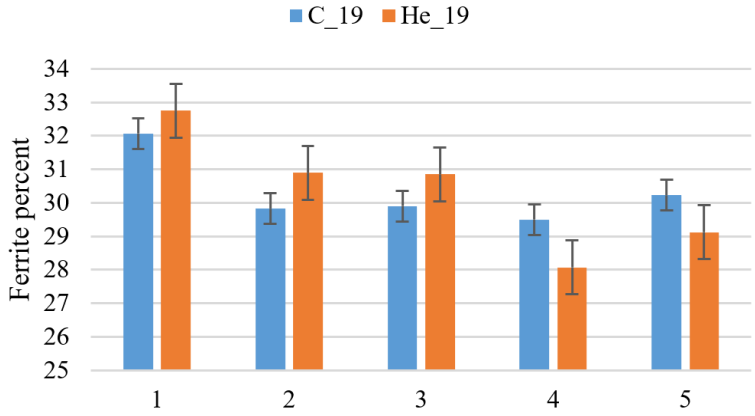

Fig. 19. Comparing the average ferrite percent on the same 19V voltage with different shielding gas by the C_19 and He_19 samples

Effect of the arc voltage

Less heat input means shorter cooling time, so the ferrite ratio of samples with lower voltage settings was expected to be higher. To examine the effect of voltage, the samples were compared and manufactured with the same parameters except for voltage.

Fig. 20 shows the ferrite content for the same shielding gas at different voltages. A higher ferrite content could be measured at lower voltages at each measurement point. The standard deviation of the ferrite percentage of the C_17 sample fell between 0.4 and 2.6, while the standard deviation of the ferrite percentage of the C_19 sample fell between 0.7 and 1.9.

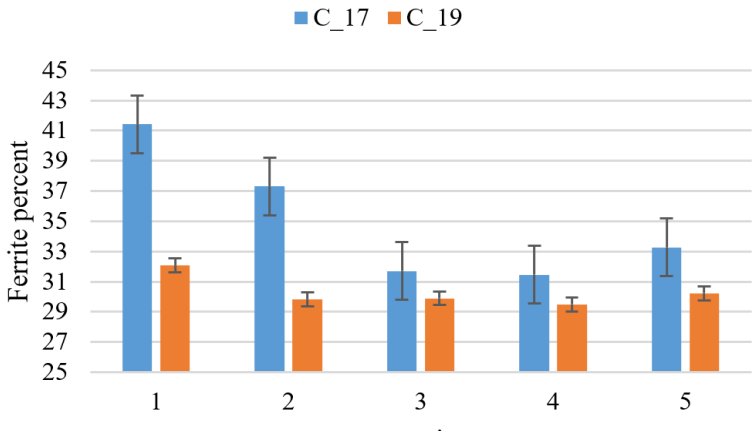

Fig. 20. Comparing the average ferrite percent on different voltages with the same shielding gas by the C_17 and C_19 samples

Observing the trend in Fig. 21 for the shielding gas with helium, the smaller austenite ratio can also be noticed in the case of 17V. This is due to the lower heat input, which caused the sample to cool down faster. The standard deviation of the ferrite percentage of the He_17 sample fell between 0.7 and 2.7, while the standard deviation of the ferrite percentage of the He_19 sample fell between 0.2 and 1.1.

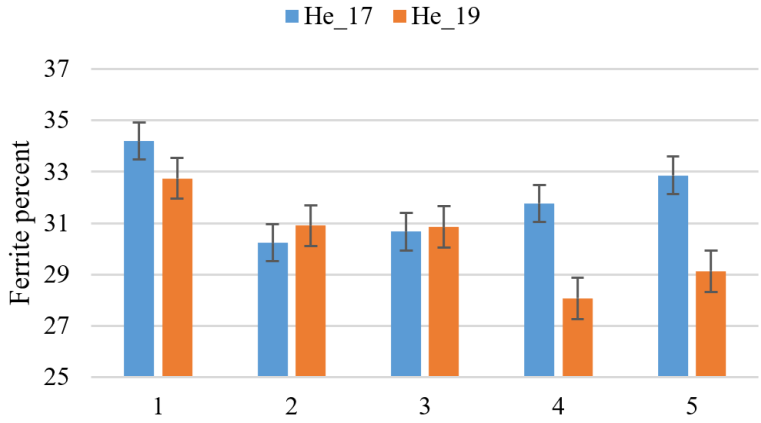

Fig. 21. Comparing the average ferrite percent on different voltages with the same shielding gas by the He_17 and He_19 samples

Results of the hardness test

As Luchtenberg et al. [34] and Weng et al. [35] previously established, the difference in hardness between the ferrite and austenite phases in duplex steels is minimal. No clear conclusions can be drawn about the microstructure from the results.

The measurement was carried out on the He_19 sample to be checked against the data found in the professional literature.

The hardness was measured in the middle of the sample along the width in the third line boxes. The application of the loading force lasted for 12 seconds. During the measurement, 84 points were recorded. There was 0.2 mm between the prints, so the requirements contained in the ISO 6507-1 standard were met in all cases. The measured hardness values are shown in Fig. 22. The diagram indicates that the standard deviation of the estimated points is significant, but compared to the 266 HV average, 85% of the values are in the range of ±9 HV.

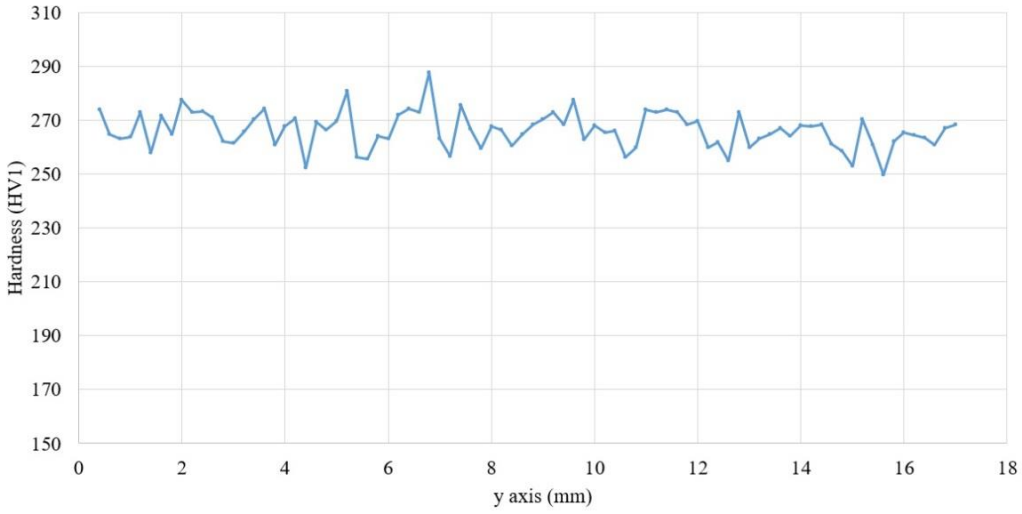

Fig. 22. The results of the hardness measurement using a 1 kg load along the width of the middle of the He_19 sample

CONCLUSIONS

In our research, 4 walls were manufactured with WAAM. Two different voltages were applied, 19V and 17V, and each voltage has two different shielding gases: the M12-ArC-2.5 and M12-ArHeC-20/2. The walls were made with G 22 9 3 NL (ER2209) wire using the WAAM method with the Yaskawa robot. The following conclusions were made:

- It was found that the Otsu method to calculate the ferrite content was more precise and provided adequate data compared to feritscope measurements. The results of comparing these two methods are not directly comparable, but the trends can be determined. The trend indicates that the ferrite rate is decreasing with the increasing number of layers. This can be attributed to the increase in height because the heat removal reduces due to the multiple layers, increasing the cooling time. It can be found that the ferrite content rises again from the 4th line of the samples. This satisfied the preliminary assumption that the ferrite content in the walls will decrease with increasing the number of layers. The decrease will slow down as thermal equilibrium is established, or the ferrite content will be almost constant. A slight increase was observed in the highest layers.
- It can be determined that the ferrite percent is higher with the M12-ArC-2.5 gas by the 17V parameter. Almost the same ferrite content can be measured by the two different gases at the voltage 19V, but in the upper layers, the wall was made with M12-ArC-2.5 gas, showing less austenite content.
- It was also found that the lower voltage caused the highest ferrite content for both gas types. As an effect of changing the parameters, it is important to emphasize that increasing the voltage is associated with an increase in the specific heat input, thus with an increase in the cooling time $\Delta t_{12/8}$ and the austenite content.
- Comparing the ferrite ratio by different welding parameters, it can be established that when He gas was used, the standard deviation of the ferrite percentage was the smallest (except one out of the 4 cases).
- The hardness measurement results proved that it is impossible to make a clear difference between the hardness of the two phases.
- It should be noted that increasing the proportion of He in the shielding gas increases the austenite content, as confirmed by several studies. Compared to argon, helium has a higher ionization energy and heat conductivity; consequently, the specific heat input increases when used as a shielding gas [36–38]. The results show that the effect of the two parameters on the microstructure cannot be evaluated separately since the effect of He was more remarkable at a lower voltage.
- According to the ISO 17781 standard, the C_17 wall parameters were appropriate, with a minimum of 30% ferrite percent. This ER 2209 duplex stainless steel can recommend these parameters for industrial applications.

ACKNOWLEDGEMENT

The Authors would like to thank Linde Gáz Magyarország Zrt. especially to Károly Abaffy and László Gyura and Flexman Robotics Kft. for the equipment and professional assistance during the manufacturing.

This paper has been supported by the National Research, Development and Innovation Office – NKFIH, OTKA PD 138729 (B. Varbai). The research reported in this paper is part of project no. TKP-6-6/PALY-2021, which has been implemented with the support provided by the Ministry of Culture and Innovation of Hungary from the National Research, Development and Innovation Fund, financed under the TKP2021-NVA funding scheme.
The publication was funded by the European Union through the ERASMUS+ Strategic Partnership Key Action 2, 2021-1-RO01-KA220-HED-000032181, ALLIES

Conflicts of Interest

The authors declare that they have no competing financial interests or personal relationships that could have seem to influence the study reported in this paper.

REFERENCES

1. J. C. Lippold, D. J. Kotecki, “Welding metallurgy and weldability of stainless steels”. John Wiley & Sons, Inc. 2005.
2. A. Baghdadchi, V. A. Hosseini, K. Hurtig, and L. Karlsson, “Promoting austenite formation in laser welding of duplex stainless steel-impact of shielding gas and laser reheating”, Weld World, vol. 65, pp. 499–511, 2021, doi: 10.1007/s40194-020-01026-7.
3. M. Landowski, “Influence of Parameters of Laser Beam Welding on Structure of 2205 Duplex Stainless Steel,” Adv Mater Sci, vol. 19, no. 1, pp. 21–31, Mar. 2019, doi: 10.2478/adms-2019-0002.
4. D. Zhang, A. Liu, B. Yin, and P. Wen, “Additive manufacturing of duplex stainless steels - A critical review,” J Manuf Proc, vol. 73. Elsevier Ltd, pp. 496–517, Jan. 01, 2022. doi: 10.1016/j.jmapro.2021.11.036.
5. A. K. Maurya, C. Pandey, and R. Chhibber, “Dissimilar welding of duplex stainless steel with Ni alloys: A review,” Int J Press Vess, vol. 192. Elsevier Ltd, Aug. 01, 2021. doi: 10.1016/j.ijpvp.2021.104439.
6. E. M. Westin and F. G. Warchomicka, “Solidification cracking in duplex stainless steel flux-cored arc welds Part 2 — susceptibility of 22Cr all-weld metals under high restraint,” Weld World, vol. 66, no. 12, pp. 2425–2442, Dec. 2022, doi: 10.1007/s40194-022-01389-z.
7. “ISO 17781:2017: Petroleum, petrochemical and natural gas industries — Test methods for quality control of microstructure of ferritic/austenitic (duplex) stainless steels.” Jul. 2017. Accessed: Oct. 01, 2023. [Online]. Available: https://www.iso.org/standard/60525.html
8. M. Landowski, A. Świerczyńska, G. Rogalski, and D. Fydrych, “Autogenous fiber laser welding of 316L austenitic and 2304 lean duplex stainless steels,” Materials, vol. 13, no. 13, pp. 1–16, Jul. 2020, doi: 10.3390/ma13132930.
9. K. U. Rani, R. Kumar, M. M. Mahapatra, R.S. Mulik, A. Świerczyńska, D. Fydrych, C. Pandey, “Wire Arc Additive Manufactured Mild Steel and Austenitic Stainless Steel Components: Microstructure, Mechanical Properties and Residual Stresses,” Materials, vol. 15, no. 20, Oct. 2022, doi: 10.3390/ma15207094.
10. “ISO 4063:2023: Welding, brazing, soldering and cutting — Nomenclature of processes and reference numbers.” International Organization for Standardization, Mar. 2023. Accessed: Oct. 01, 2023. [Online]. Available: https://www.iso.org/standard/75108.html
11. C. R. Cunningham, J. M. Flynn, A. Shokrani, V. Dhokia, and S. T. Newman, “Invited review article: Strategies and processes for high quality wire arc additive manufacturing,” Addit Manuf, vol. 22., pp. 672–686, Aug. 01, 2018. doi: 10.1016/j.addma.2018.06.020.

12. M. A. Jackson, A. Van Asten, J. D. Morrow, S. Min, and F. E. Pfefferkorn, "A Comparison of Energy Consumption in Wire-based and Powder-based Additive-subtractive Manufacturing," in Proc Manuf, 2016, pp. 989–1005. doi: 10.1016/j.promfg.2016.08.087.
13. D. Ding, Z. Pan, D. Cuiuri, and H. Li, "Wire-feed additive manufacturing of metal components: technologies, developments and future interests," Int J Adv Manuf Technol, vol. 81, no. 1–4. Springer London, pp. 465–481, Oct. 26, 2015. doi: 10.1007/s00170-015-7077-3.
14. A. Taşdemir and S. Nohut, "An overview of wire arc additive manufacturing (WAAM) in shipbuilding industry," Ships Offshore Struct, pp. 1–18, 2020. doi: 10.1080/17445302.2020.1786232.
15. J. Łabanowski, K. Prokop-Strzelczyńska, G. Rogalski, and D. Fydrych, "The Effect of Wet Underwater Welding on Cold Cracking Susceptibility of Duplex Stainless Steel," Adv Mater Sci, vol. 16, no. 2, pp. 68–77, Jun. 2016, doi: 10.1515/adms-2016-0010.
16. P. R. Seré, C. Deyá, C. I. Elsner, and A. R. Di Sarli, "Behavior of two eco-compatible duplex systems used in the construction industry against corrosion," Int J Adhes Adhes, vol. 50, pp. 1–6, Apr. 2014, doi: 10.1016/j.ijadhadh.2013.12.019.
17. M. Eriksson, M. Lervåg, C. Sørensen, A. Robertstad, B. M. Brønstad, B. Nyhus, R. Aune, X. Ren, O. M. Akselsen, "Additive manufacture of superduplex stainless steel using WAAM," in MATEC Web Conf, EDP Sciences, Aug. 2018. doi: 10.1051/matecconf/201818803014.
18. V. A Hosseini, M. Högström, K. Hurtig, M. A. Valiente Bermejo, L. E. Stridh, and L. Karlsson, "Wire-arc additive manufacturing of a duplex stainless steel: thermal cycle analysis and microstructure characterization," Weld World, vol. 63, no. 4, pp. 975–987, Jun. 2019, doi: 10.1007/s40194-019-00735-y.
19. N. Knezović, I. Garašić, and I. Jurić, "Influence of the interlayer temperature on structure and properties of wire and arc additive manufactured duplex stainless steel product," Materials, vol. 13, no. 24, pp. 1–16, Dec. 2020, doi: 10.3390/ma13245795.
20. X. Bi, R. Li, Z. Hu, J. Gu, and C. Jiao, "Microstructure and Texture of 2205 Duplex Stainless Steel Additive Parts Fabricated by the Cold Metal Transfer (CMT) Wire and Arc Additive Manufacturing (WAAM)," Metals (Basel), vol. 12, no. 10, Oct. 2022, doi: 10.3390/met12101655.
21. A. Queguineur, R. Asadi, M. Ostolaza, E. H. Valente, V. K. Nadimpalli, G. Mohanty, J.-Y. Hascoët, I. F. Ituarte, "Wire arc additive manufacturing of thin and thick walls made of duplex stainless steel," Int J Adv Manuf Technol, vol. 127, no. 1–2, pp. 381–400, Jul. 2023, doi: 10.1007/s00170-023-11560-5.
22. Y. Zhang, F. Cheng, and S. Wu, "The microstructure and mechanical properties of duplex stainless steel components fabricated via flux-cored wire arc-additive manufacturing," J Manuf Process, vol. 69, pp. 204–214, Sep. 2021, doi: 10.1016/j.jmapro.2021.07.045.
23. "ISO 14343:2017: Welding consumables — Wire electrodes, strip electrodes, wires and rods for arc welding of stainless and heat resisting steels — Classification," International Organization for Standardization, Mar. 2017, Accessed: Oct. 01, 2023. [Online]. Available: https://www.iso.org/standard/67727.html
24. "ISO 14175:2008: Welding consumables — Gases and gas mixtures for fusion welding and allied processes," International Organization for Standardization, Oct. 2008, Accessed: Oct. 01, 2023. [Online]. Available: https://www.iso.org/standard/39569.html
25. Linde Gáz Magyarország Zrt., "Védőgázok - A Linde hegesztési védőgázai," Version: v.17.
26. Alleima, "Shielding gas recommendations for MIG and TIG welding," https://www.alleima.com/en/technical-center/shielding-the-weld/. Accessed: Sep. 04, 2023. [Online]. Available: https://www.alleima.com/en/technical-center/shielding-the-weld/

27. Certilas, “The filler metal specialist: Duplex 2209 stainless steels welding wire. Type 2219, 1.4462.” Accessed: Sep. 04, 2023. [Online]. Available: https://certilas.com/en/product/2209-duplex

28. M. Koukolíková, P. Podaný, S. Rzepa, M. Brázda, and A. Kocijan, “Additive manufacturing multi-material components of SAF 2507 duplex steel and 15-5 PH martensitic stainless steel,” J Manuf Process, vol. 102, pp. 330–339, Sep. 2023, doi: 10.1016/j.jmapro.2023.07.057.

29. B. Bögre and I. Mészáros, “Problems of ferrite content determination,” Period Polytech Mech Eng, vol. 64, no. 2, pp. 150–158, 2020, doi: 10.3311/PPME.15022.

30. “ISO 6507-1:2018: Metallic materials — Vickers hardness test — Part 1: Test method,” International Organization for Standardization. Jan. 2018. Accessed: Oct. 01, 2023. [Online]. Available: https://www.iso.org/standard/64065.html

31. N. Otsu, “A_Threshold_Selection_Method_from_Gray-Level_Histograms,” IEEE Trans Syst Man Cybern. Syst, 9, 62-66, 1979, doi: 10.1109/TSMC.1979.4310076

32. X. Zhang, K. Wang, Q. Zhou, J. Kong, Y. Peng, J. Ding, C. Diao, D. Yang, Y. Huang, T. Zhang, S. W. Williams, “Element partitioning and electron backscatter diffraction analysis from feeding wire to as-deposited microstructure of wire and arc additive manufacturing with super duplex stainless steel,” Mater Sci Eng A, vol. 773, Jan. 2020, doi: 10.1016/j.msea.2019.138856.

33. L. Karlsson, “Welding duplex stainless steels – A review of current recommendations”, Welding in the World, vol. 56, 2012

34. P. Luchtenberg, P. T. de Campos, P. Soares, C. A. H. Laurindo, O. Maranho, and R. D. Torres, “Effect of welding energy on the corrosion and tribological properties of duplex stainless steel weld overlay deposited by GMAW/CMT process,” Surf Coat Technol, vol. 375, pp. 688–693, Oct. 2019, doi: 10.1016/j.surfcoat.2019.07.072.

35. K. L. Weng, H. R. Chen, and J. R. Yang, “The low-temperature aging embrittlement in a 2205 duplex stainless steel,” Mater Sci Eng A, vol. 379, no. 1–2, pp. 119–132, Aug. 2004, doi: 10.1016/j.msea.2003.12.051.

36. K. Korjala, “Helium as a welding shielding gas: Effects on CO_2 emissions by helium recovery and recycling system,” Licentiate Thesis, Lappeenranta-Lahti University of Technology LUT, Finland, 2021, URN: NBN:fi-fe2021062840210

37. Z. H. Rao, J. Hu, S. M. Liao, and H. L. Tsai, “Modeling of the transport phenomena in GMAW using argon-helium mixtures. Part i - The arc,” Int J Heat Mass Transf, vol. 53, no. 25–26, pp. 5707–5721, Dec. 2010, doi: 10.1016/j.ijheatmasstransfer.2010.08.009.

38. A. Fellman and V. Kujanpää, “The effect of shielding gas composition on welding performance and weld properties in hybrid CO_2 laser–gas metal arc welding of carbon manganese steel,” J Laser Appl, vol. 18, no. 1, pp. 12–20, Feb. 2006, doi: 10.2351/1.2164481.